Quantitative Magneto-Mechanical Detection and Control of the Barkhausen Effect

J. A. J. Burgess *et al.*

Science **339**, 1051 (2013);
DOI: 10.1126/science.1231390

7. J. Smak, *Acta Astronom.* **19**, 155 (1969).
8. J. A. Orosz, C. D. Bailyn, R. A. Remillard, J. E. McClintock, C. B. Foltz, *Astrophys. J.* **436**, 848 (1994).
9. J. A. Orosz, C. D. Bailyn, *Astrophys. J.* **446**, L59 (1995).
10. See the supplementary materials on *Science* Online.
11. V. Kalogera, G. Baym, *Astrophys. J.* **470**, L61 (1996).
12. N. E. White, K. O. Mason, *Space Sci. Rev.* **40**, 167 (1985).
13. S. B. Foulkes, C. A. Haswell, J. R. Murray, *Mon. Not. R. Astron. Soc.* **366**, 1399 (2006).
14. J. M. Bardeen, J. A. Petterson, *Astrophys. J.* **195**, L65 (1975).
15. J. Lense, H. Thirring, *Phys. Z.* **19**, 156 (1918).
16. A. Ingram, C. Done, P. C. Fragile, *Mon. Not. R. Astron. Soc.* **397**, L101 (2009).
17. A. King, in *X-ray Binaries*, W. H. G. Lewin, J. van Paradijs, E. P. J. van den Heuvel, Eds. (Cambridge Univ. Press, Cambridge, 1997), p. 419.
18. J. A. de Jong, J. van Paradijs, T. Augusteijn, *Astron. Astrophys.* **314**, 484 (1996).
19. J. Frank, A. R. King, J.-P. Lasota, *Astron. Astrophys.* **178**, 137 (1987).
20. J. van Paradijs, M. van der Klis, H. Pedersen, *Astron. Astrophys. Suppl. Ser.* **76**, 185 (1988).
21. M. Armas-Padilla, N. Degenaar, D. M. Russell, R. Wijnands, *Mon. Not. R. Astron. Soc.* **428**, 3083 (2013).
22. J. van Paradijs, J. E. McClintock, in *X-ray Binaries*, W. H. G. Lewin, J. van Paradijs, E. P. J. van den Heuvel, Eds. (Cambridge Univ. Press, Cambridge, 1997), p. 58.
23. M. Milgrom, *Astron. Astrophys.* **67**, L25 (1978).
24. R. Antonucci, *Astron. Astrophys. Ann. Rev.* **31**, 473 (1993).
25. J. E. McClintock, R. A. Remillard, in *Compact Stellar X-ray Sources*, W. H. G. Lewin, M. van der Klis, Eds. (Cambridge Univ. Press, Cambridge, 2006), p. 157.
26. H. A. Krimm, J. A. Kennea, S. T. Holland, *The Astronomer's Telegram* **3142**, 1 (2011).
27. G. R. Sivakoff, J. C. A. Miller-Jones, H. A. Krimm, *The Astronomer's Telegram* **3147**, 1 (2011).
28. M. Livio, G. I. Ogilvie, J. E. Pringle, *Astrophys. J.* **512**, 100 (1999).
29. D. L. Meier, *Astrophys. J.* **548**, L9 (2001).
30. G. Ponti *et al.*, *Mon. Not. R. Astron. Soc.* **422**, L11 (2012).
31. H. A. Krimm *et al.*, *The Astronomer's Telegram* **3138**, 1 (2011).
32. A. R. King, R. Wijnands, *Mon. Not. R. Astron. Soc.* **366**, L31 (2006).

Acknowledgments: This work made use of the Image Reduction and Analysis Facility (IRAF) and the MOLLY software developed by T. R. Marsh. We thank P. Charles, G. Ponti, and D. M. Russell for their useful comments; G. Pérez and M. Leal for their help with fig. S3 and movie S1; and I. Negueruela and C. González-Fernández for obtaining the Intermediate Dispersion Spectrograph (IDS) spectra. Based on observations made with the INT and WHT, operated by the Isaac Newton Group; the LT, operated by the Liverpool John Moores University with financial support from the UK Science and Technology Facilities Council; and the MT, operated by the University of Leuven and the Observatory of Geneva. All of them are installed at the Spanish Observatorio del Roque de Los Muchachos (on the island of La Palma) of the Instituto de Astrofísica de Canarias (IAC). The photometry taken on 26 April 2011 is based on observations made with the INT under the Spanish IAC Director's Discretionary Time. T.M.D. acknowledges funding via a European Union Marie Curie Intra-European Fellowship under contract no. 2011-301355. This research was supported by the Spanish Ministerio de Ciencia e Innovación (MICINN) under grant AYA2010-18080 and partly funded by the Spanish MICINN under the Consolider-Ingenio 2010 Program grant CSD2006-00070: "First science with the GTC" (www.iac.es/consolider-ingenio-gtc/).

Supplementary Materials

www.sciencemag.org/cgi/content/full/339/6123/1048/DC1
Supplementary Text
Figs. S1 to S3
Table S1
References (*33*–*50*)
Movie S1

31 July 2012; accepted 20 December 2012
10.1126/science.1228222

Quantitative Magneto-Mechanical Detection and Control of the Barkhausen Effect

J. A. J. Burgess,[1,2] A. E. Fraser,[1] F. Fani Sani,[1,2] D. Vick,[2] B. D. Hauer,[1] J. P. Davis,[1,2] M. R. Freeman[1,2]*

Quantitative characterization of intrinsic and artificial defects in ferromagnetic structures is critical to future magnetic storage based on vortices or domain walls moving through nanostructured devices. Using torsional magnetometry, we observe finite size modifications to the Barkhausen effect in the limiting case of a single vortex core interacting with individual pointlike pinning sites in a magnetic thin film. The Barkhausen effect in this limit becomes a quantitative two-dimensional nanoscale probe of local energetics in the film. Tailoring the pinning potential using single-point focused ion beam implantation demonstrates control of the effect and points the way to integrated magneto-mechanical devices incorporating quantum pinning effects.

The Barkhausen effect refers to the stochastic jumps in magnetization resulting from the pinning of magnetic domain patterns (*1*). Of current interest is how the phenomenon is modified at the smallest scale and the consequent technological implications. Thin-film magnetic disks exhibit a ground-state vortex (*2*–*4*) and offer a convenient platform to study a single vortex core. The magnetic vortex core is equivalent to a zero-dimensional domain wall and is often restricted to a radius of less than 10 nanometers (*5*). The high density of exchange energy within the core enhances local interactions (*6*–*8*). A single pointlike pinning site, together with a vortex core, constitutes the simplest system to exhibit the Barkhausen effect. Previous work has shown indirect signs of the Barkhausen effect for the vortex state. Local variation in films has been found to cause a stick-slip motion (*9*) and to increase the frequencies of dynamic modes of the vortex (*10*–*13*).

Technologically, domain-wall pinning, and consequently Barkhausen effects, present an opportunity to enhance spintronic memory (*14*) and construct magnetic logic devices (*15*, *16*). In wire geometries, film imperfections affect domain-wall velocity and energy loss (*17*), whereas thermal motion of wall structures in wire kinks has been exploited to learn about nonadiabatic spin torque (*18*). Artificial control of pinning potentials will be important for device applications (*16*), and focused ion beam modification (*19*) is emerging as a leading technique.

Nanomechanical torque magnetometry (*20*, *21*) provides an ideal method of measuring minute magnetization (M) changes with minimal influence on the sample (Fig. 1A). The device is constructed as a paddle supported by thin rods that act as a torsion spring. A single 1-μm-diameter, 42-nm-thick, permalloy disk exhibiting a vortex ground state is fabricated on the paddle. As the field (H) is increased, the vortex core is deflected orthogonally to the field direction, moving it through the film. This permits a torque to be applied to the in-plane magnetic moment by an out-of-plane field, inducing a deflection of the paddle linearly proportional to the magnetization. The deflection is measured by a laser interferometer (*21*). Energetic interactions between the core and imperfections in the film—thickness variations, grain boundaries, or material impurities—alter the energy cost of shifting the core, leading to concomitant variations in the differential magnetic susceptibility, dM/dH (Fig. 1B). During pinning, the differential susceptibility is suppressed but, crucially, does not vanish, whereas transitions between pinning sites appear as steep sections.

At room temperature all intersite transitions appear continuous and reversible; however, at $T = 77$ K, some transition states become minor hysteresis loops. Bistable states are masked at room temperature by thermally activated intersite hopping. When the hopping rate exceeds the measurement bandwidth (~30 Hz), a time-averaged magnetization, weighted by the occupancy of the participating states, is recorded. Investigation at intermediate temperatures shows the convergence of the experimental bandwidth and the hopping frequency as the thermal noise slows (Fig. 2A). This makes the mechanism for the emergence of hysteresis at low temperature clear. Stopping at fixed fields around the hysteresis loop allows traces of Barkhausen telegraph noise to be captured (Fig. 2B). Incrementing the field demonstrates that the lifetimes of the states have strong field dependence. Computation of the lifetimes of the states from telegraph noise

[1]Department of Physics, University of Alberta, 4-181 Centennial Centre for Interdisciplinary Science, Edmonton, Alberta T6G 2E1, Canada. [2]National Institute for Nanotechnology, 11421 Saskatchewan Drive, Edmonton, Alberta T6G 2M9, Canada.

*To whom correspondence should be addressed. E-mail: mark.freeman@ualberta.ca

traces enables calculation of hopping energy barriers for varied temperatures and fields. An Arrhenius relation is used to describe the dynamics $\tau = f_o^{-1} \exp(\Delta E/k_B T)$ (with f_o = 200 MHz approximating the gyrotropic mode frequency). For separate data runs, the measured energy barrier and hysteresis loop position change slightly, indicating very fine scale instability in the hopping pathway. In the example traces shown in Fig. 2C, the barrier at which occupancy of the two sites is equal is found to be ~0.14 eV in the 80- and 90-K traces, whereas it is ~0.1 eV in the 60-K trace.

In a perfect disk, the deflection of the core by the applied bias field would lead to a straight path orthogonal to the field. However, the imperfections that introduce pinning and telegraph noise present the possibility of two-dimensional (2D) path deviations from the ideal path. Adding a second in-plane orthogonal field, H_y, to the primary bias field, H_x, allows 2D measurements (Fig. 3A). Using secondary field values equivalent to path shifts on the nanometer scale to explore a prominent minor hysteresis loop shows the strong influence of the 2D distribution. On the low-field side of the loops, a single site with a clear circular interaction profile dominates. On the high-field side, multiple pinning sites can be identified by counting the distinct magnetization levels in the minor hysteresis loops.

To perform a quantitative analysis of the *M-H* curves in 1D and 2D, a deformable vortex pinning model was developed (*22*, *23*) based on the rigid vortex model (*24*, *25*) and the two-vortex model (*26*, *27*). This model captures the field dependence of both the core position and the flexing of the disk magnetization in response to the presence of imperfections, whether they are strong enough to locally trap the vortex or merely modify its progression across the disk (*22*) (fig. S3). More details are in the supplementary materials (*22*) and in (*23*), which also contains extensive evaluation of model performance against micromagnetic simulation. The model may be applied by fitting to the measured magnetization data, enabling the extraction of a quantitative pinning potential. Consequently, this allows computation of potential energy barriers separating bistable states and the associated thermal dynamics. The steps necessary to accurately fit the model to the data are described in the supplementary materials (*22*). This fitting approach is applied to Fig. 1B to extract a quantitative

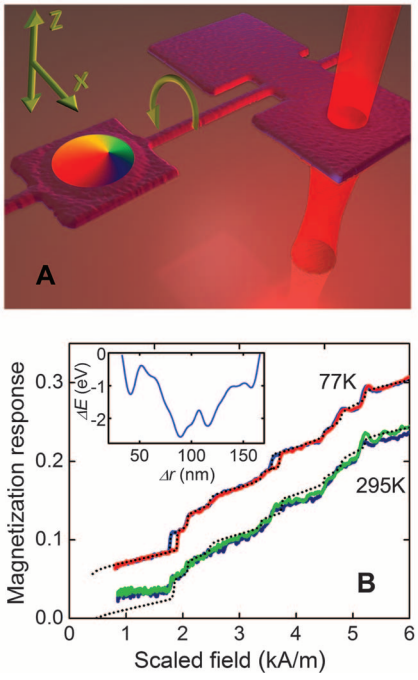

Fig. 1. Device schematic and magnetization curves showing the Barkhausen effect. (**A**) A silicon nitride nanomechanical torque magnetometer holding a ferromagnetic disk is read out using laser interferometry. Inducing magnetization with a static field in-plane (along *x*) and applying an AC out-of-plane (*z*) field drives the torsional resonance of the paddle with an amplitude proportional to the magnetization. (**B**) Low-field *M-H* loops show the influence of pinning sites on *dM/dH*. At 77 K, bistable states appear in the up (red) and down (blue) sweeps, and at 295 K (offset for clarity) up (green) and down (blue) sweeps are identical. Magnetic field is rescaled as $H_{scaled} = H\,[M_S(T = 0)/M_S(T)]$ to normalize the field position of features independently of temperature (*25*, *31*). An analytic fit (dotted line), including thermal effects (*22*), to the 77-K data is used to extract the disorder potential (inset). Recomputing using the same potential at room temperature, the hopping rates exceed the measurement bandwidth and mask the bistability.

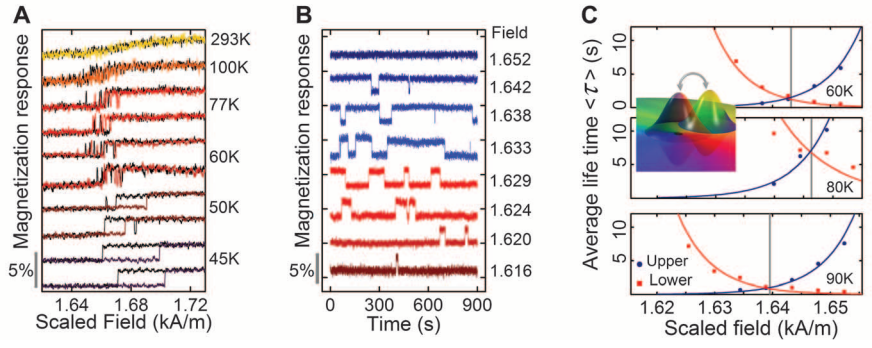

Fig. 2. Barkhausen telegraph noise across a bistable transition. (**A**) The strong temperature dependence of minor hysteresis is probed over a bistable state (the first minor loop in Fig. 1B) with a field sweep rate of 0.45 $Am^{-1}s^{-1}$. (**B**) At 77 K and various fixed fields (labeled in kA/m), telegraph noise traces show strong field dependence. The gray bar indicates the normalized magnetization scale. (**C**) For three temperatures the average lifetimes of the upper and lower states are calculated as a function of field using an Arrhenius fit to the observed lifetime distribution of telegraph noise traces. Analytical estimates of the lifetimes computed from the vortex pinning model show that the two sites are separated by ~10 nm in *y*. For equal state occupancy, the barriers range between 100 and 140 meV. The inset is a cartoon depicting the hopping process.

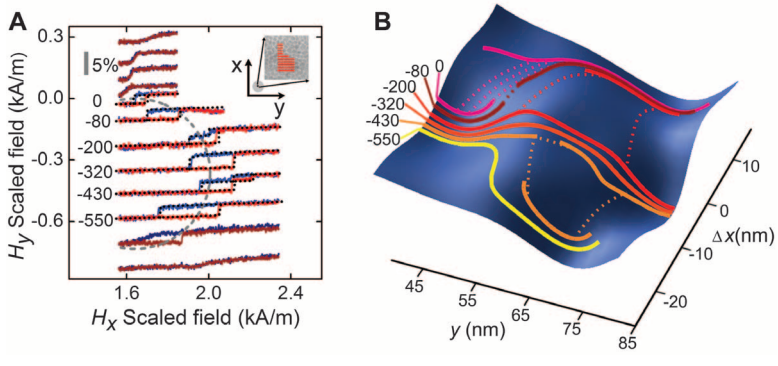

Fig. 3. Quantitative 2D mapping of the pinning potential. (**A**) Field sweeps taken with various secondary, H_y, field values (labeled in A/m) probe the landscape around a strong pinning site. The circular profile of the central site is clearly visible; a dashed line indicates a circle with radius 10 nm computed analytically, assuming no pinning. The inset is a cartoon of the idealized paths overlaid on a representative 50-nm-square transmission electron microscopy (TEM) image showing the grain structure of the permalloy disk. The gray bar indicates the normalized magnetization scale. (**B**) A 2D potential is constructed that yields minimum energy paths (solid lines) and estimated hopping trajectories (dashed lines) with profiles matching those extracted from the hysteresis loops in (A). The field values are labeled in A/m. For the $H_y = 0$ path, the broad overlap of bistable paths provides a multitude of diagonal hopping paths with energy barriers in the 100- to 200-meV range, consistent with Fig. 2C.

potential as a function of the real, pinned position of the core. Typical pinning site energies between 0.6 and 2.0 eV are found. Fitting to the measured field evolution of the state lifetimes shown in Fig. 2C results in two pinning sites spaced out by approximately 10 nm with a steep barrier. Considering the size limitations on energetic profiles imposed by the core, this implies a diagonal hopping path.

Analysis in 2D presents additional challenges. For any single magnetization trace, the potential extracted is a 1D projection of the defect potential encountered along the 2D path of minimum energy (*22*) (fig. S4). From each loop shown in Fig. 3A, a 1D potential was extracted. Subsequently, a 2D potential (Fig. 3B) was constructed that yields minimum-energy path profiles that match each extracted 1D potential when the appropriate secondary, H_y, field value is included. The details of constraining the constructed 2D potential can be found in the supplementary materials (*22*). This provides an estimate of the 2D pinning site distribution probed by the vortex core.

A better idea of the morphology of the natural pinning may be gleaned from the 2D data. The strongest individual sites used in the reconstruction are 2.0 to 2.5 eV deep, whereas the weakest are ~0.3 eV, corroborating the range found in the 1D fit. Site sizes range from 7 to 10 nm in standard deviation, matching closely with the 7.3-nm standard deviation of the simulated exchange energy distribution of a vortex core in this size of disk (fig. S5). Any defect profile will be convolved with the energy profile of the core, indicating that the pinning sites are typically very small, effectively pointlike up to a few nanometers in width.

The minimum energy paths in the 2D constructed potential shown in Fig. 3B reveal the complexity of the situation. Minor hysteresis can arise for transitions between bistable positions along the same path or between separate paths. Both types of hopping are observed. The existence of two paths raises the possibility of hysteresis loops where the path on the sweep up is different from that on the sweep down. This is seen in Fig. 3A in the $H_y = -430$ A/m and $H_y = -200$ A/m loops, where the computed paths imply that the core traverses one side of the repulsive site on the sweep up and the other side on the sweep down. Near $H_y = 0$ ($x = 0$, $y =$ 50 nm), a variety of low-barrier (100 to 200 meV) hopping trajectories exist between paths. The diagonal hopping trajectories accessible are consistent with the field values and variability observed in the hopping (Fig. 2C), as are the barrier heights and site separations. The complexity of the paths leads to the richness of features exhibited in the minor loops in Fig. 3A. Conversely, only by considering every subtle feature and change between adjacent hysteresis loops is the reconstruction of the 2D potential possible. The hysteresis and analytical modeling approach presented here is compatible with dynamical pinning techniques (*10*, *11*, *13*), and a combined study could extract complementary measurements of potential well shapes with additional information, such as local dissipation.

The detailed understanding of the quasistatic and low-speed stochastic dynamics of the vortex core in its natural pinning potential motivates detailed exploration of artificial texturing of the local magnetic energy to create magneto-mechanical devices. The concept is demonstrated by the addition of three stronger pinning sites introduced by ion milling fine dimples into the surface. Very low current (0.3 pA), fast-shuttered (40 ms) point exposures of a focused gallium ion beam (~70,000 Ga^+ ions) were used (*22*). This is a very much scaled-down version of the creation of artificial pinning sites as holes through the disk that eliminate the vortex core (*28*, *29*). Here, the vortex core is maintained but reduced in energetic cost by the ion damage. Ion damage–based sites, in principle, are continuously adjustable starting from zero pinning strength. Here, one dimple was placed ~110 nm from the disk center, whereas on the opposite side of the disk two dimples were placed at ~200 and 280 nm to enable identification of the chirality of the vortex state. All dimples were placed along the y axis, where previous measurements had characterized the natural pinning potential. The modified magnetization response as the core passes through the pinning site is shown in Fig. 4A. Even at room temperature, strong minor hysteresis loops mark the entrance and exit points of the core from the dimple. Exploring the opposite side of the disk, similarly dramatic changes occur (Fig. 4B), including clean minor hysteresis from direct transitions between the proximal dimples, as seen with dual holes (*28*). Applying the model, good fits are found for Gaussian pinning sites at 110, 215, and 300 nm, with depths between 17 and 21 eV and a common standard deviation of 18 nm. This pinning site strength is equivalent to the complete suppression of magnetization in a volume equivalent to a cylinder ~6 nm in radius through the thickness of the disk. The physical thinning of the disk at the dimple, ~2 nm depth by atomic force microscopy (fig. S2), or dilution of magnetic material by Ga is insufficient. This suggests that the Ga^+ ions disrupt the exchange interaction. Assuming linear response, the efficacy of magnetic potential well excavation is ~0.3 meV per implanted ion. In this polycrystalline sample, artificial pinning sites down to the natural energetic corrugation will remain detectable. However, in a single crystal sample, energetic scales well below this should be accessible. Variable strength of pinning with preservation of the core structure indicates the possibility for pointillist rendering of a full, quantitative 2D energy landscape. Recent work demonstrates the applicability of very weak gradient dose pinning (*16*).

The technological potential of controlled magnetic pinning spans applications from spin transfer oscillator devices to integrated magneto-mechanical memories. With demonstrated sensitivities for measurement and modification that extrapolate to the meV level, the techniques for characterization and control reported here offer a route all the way down to the range of artificial corrugations relevant to quantum devices exploiting tunneling of the magnetization (*30*).

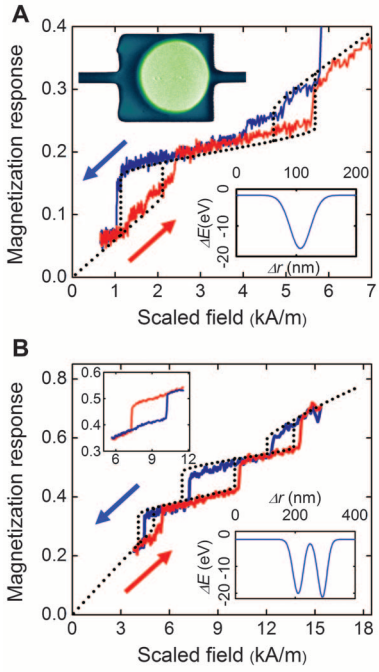

Fig. 4. Control of the Barkhausen effect. (**A**) Point exposures of Ga^+ ions disrupt ordering in the permalloy film, creating strongly interacting artificial pinning sites. The three added pinning sites are visible with a linear remapping of the grayscale to a color scale in a contrast-enhanced scanning electron microscopy image of the torsional paddle (inset, top left). The modified magnetization response exhibits prominent hysteresis between the up (red) and down (blue) field sweeps as the vortex is driven over the single dimple. The observed pinning is modeled accurately (dotted black line) by a Gaussian pinning potential (inset, bottom right). (**B**) The double dimple also shows strong artificially induced bistability, including hysteretic transitions directly from dimple to dimple (inset, top left). The two dimples may be modeled as Gaussian sites (inset, bottom right) with width and depths very similar to the single dimple.

References and Notes

1. H. Barkhausen, *Phys. Z.* **20**, 401 (1919).
2. R. P. Cowburn, D. K. Koltsov, A. O. Adeyeye, M. E. Welland, D. M. Tricker, *Phys. Rev. Lett.* **83**, 1042 (1999).
3. J. Raabe, R. Pulwey, R. Sattler, T. Schweinböck, J. Zweck, D. Weiss, *J. Appl. Phys.* **88**, 4437 (2000).
4. T. Shinjo, T. Okuno, R. Hassdorf, K. Shigeto, T. Ono, *Science* **289**, 930 (2000).
5. A. Wachowiak *et al.*, *Science* **298**, 577 (2002).
6. H. Min, R. D. McMichael, J. Miltat, M. D. Stiles, *Phys. Rev. B* **83**, 064411 (2011).
7. D. Toscano, S. A. Leonel, R. A. Dias, P. Z. Coura, B. V. Costa, *J. Appl. Phys.* **109**, 076104 (2011).
8. F. A. Apolonio, W. A. Moura-Melo, F. P. Crisafuli, A. R. Pereira, R. L. Silva, *J. Appl. Phys.* **106**, 084320 (2009).
9. T. Uhlig *et al.*, *Phys. Rev. Lett.* **95**, 237205 (2005).

10. R. L. Compton, P. A. Crowell, *Phys. Rev. Lett.* **97**, 137202 (2006).
11. R. L. Compton, T. Y. Chen, P. A. Crowell, *Phys. Rev. B* **81**, 144412 (2010).
12. J. S. Kim *et al.*, *Phys. Rev. B* **82**, 104427 (2010).
13. T. Y. Chen, A. T. Galkiewicz, P. A. Crowell, *Phys. Rev. B* **85**, 180406 (2012).
14. S. S. P. Parkin, M. Hayashi, L. Thomas, *Science* **320**, 190 (2008).
15. D. A. Allwood *et al.*, *Science* **309**, 1688 (2005).
16. J. H. Franken, H. J. M. Swagten, B. Koopmans, *Nat. Nanotechnol.* **7**, 499 (2012).
17. H. Min, R. D. McMichael, M. J. Donahue, J. Miltat, M. D. Stiles, *Phys. Rev. Lett.* **104**, 217201 (2010).
18. M. Eltschka *et al.*, *Phys. Rev. Lett.* **105**, 056601 (2010).
19. C. Chappert *et al.*, *Science* **280**, 1919 (1998).
20. J. Moreland, *J. Phys. D Appl. Phys.* **36**, R39 (2003).
21. J. P. Davis *et al.*, *J. Appl. Phys.* **109**, 07D309 (2011).
22. Supplementary materials are available on *Science* Online.
23. J. A. J. Burgess, J. E. Losby, M. R. Freeman, http://arxiv.org/abs/1208.3797 (2012).
24. K. Y. Guslienko, V. Novosad, Y. Otani, H. Shima, K. Fukamichi, *Phys. Rev. B* **65**, 024414 (2001).
25. J. A. J. Burgess *et al.*, *Phys. Rev. B* **82**, 144403 (2010).
26. K. Y. Guslienko *et al.*, *J. Appl. Phys.* **91**, 8037 (2002).
27. K. L. Metlov, K. Y. Guslienko, *J. Magn. Magn. Mater.* **242**, 1015 (2002).
28. M. Rahm, J. Stahl, W. Wegscheider, D. Weiss, *Appl. Phys. Lett.* **85**, 1553 (2004).
29. M. Rahm, R. Höllinger, V. Umansky, D. Weiss, *J. Appl. Phys.* **95**, 6708 (2004).
30. R. Zarzuela, S. Vélez, J. M. Hernandez, J. Tejada, V. Novosad, *Phys. Rev. B* **85**, 180401 (2012).
31. G. Mihajlovic *et al.*, *Appl. Phys. Lett.* **96**, 112501 (2010).

Acknowledgments: This work was supported by the Natural Sciences and Engineering Research Council, Canada, the Canadian Institute for Advanced Research, the Informatics Circle of Research Excellence, Canada Research Chairs, the Integrated Nanosystems Research Facility, the Canadian Foundation for Innovation, nanoAlberta, and the National Institute for Nanotechnology. The samples were fabricated using the electron microscopy facilities of the National Institute for Nanotechnology and Infrastructure of the Centre for Nanoscale Physics and Nanomaterials Research at the University of Alberta. J.B. thanks the Alberta Ingenuity Foundation/Alberta Innovates for support. We are grateful to W. Hiebert, J. Losby, Z. Diao, M. Malac, and V. Sauer for many discussions; to P. Li for TEM work; and to D. Fortin for technical assistance.

Supplementary Materials

www.sciencemag.org/cgi/content/full/science.1231390/DC1
Materials and Methods
Supplementary Text
Figs. S1 to S7
Movies S1 to S3
References (*32*–*40*)

11 October 2012; accepted 17 December 2012
Published online 17 January 2013;
10.1126/science.1231390

Coherence and Indistinguishability of Single Electrons Emitted by Independent Sources

E. Bocquillon,[1] V. Freulon,[1] J.-M Berroir,[1] P. Degiovanni,[2] B. Plaçais,[1] A. Cavanna,[3] Y. Jin,[3] G. Fève[1]*

The on-demand emission of coherent and indistinguishable electrons by independent synchronized sources is a challenging task of quantum electronics, in particular regarding its application for quantum information processing. Using two independent on-demand electron sources, we triggered the emission of two single-electron wave packets at different inputs of an electronic beam splitter. Whereas classical particles would be randomly partitioned by the splitter, we observed two-particle interference resulting from quantum exchange. Both electrons, emitted in indistinguishable wave packets with synchronized arrival time on the splitter, exited in different outputs as recorded by the low-frequency current noise. The demonstration of two-electron interference provides the possibility of manipulating coherent and indistinguishable single-electron wave packets in quantum conductors.

As with photons, the wave-particle duality plays a crucial role in the propagation of electrons in quantum conductors. The wave nature of electrons can be revealed in interference experiments (*1*–*3*) probing the single-particle coherence of electron sources through the measurement of the average electrical current. The corpuscular nature of charge carriers is apparent when measuring fluctuations of the electrical current (*4*). Yet, some experiments cannot be understood within the wave or the corpuscular description. This is the case when two-particle interference effects related to the exchange between two indistinguishable particles take place. Such experiments have proven particularly interesting—both from a fundamental standpoint, as they require a full quantum treatment, and because the on-demand generation of indistinguishable partners is at the heart of quantum information protocols (*5*). Information coding in few-electron states that propagate ballistically in quantum conductors (*6*) thus requires the production of coherent and indistinguishable single-particle wave packets emitted by several synchronized but otherwise independent emitters. The collision of two particles emitted at two different inputs of a beam splitter can be used to measure their degree of indistinguishability. In the case of bosons, indistinguishable partners always exit in the same output (Fig. 1). Fermionic statistics leads to the opposite behavior: Particles exit in different outputs. The bunching of indistinguishable photons has been observed by recording the coincidence counts between two detectors placed at the outputs of the beam splitter as a function of the time delay τ between the arrival times of the photons on the splitter. Bunching shows up in a dip in the coincidence counts, the Hong-Ou-Mandel (HOM) dip (*7*), when τ is varied. The reduction of the coincidence counts directly measures the overlap between the single-particle states at the input. It is maximum when the arrivals are synchronized and can be suppressed when the delay becomes larger than the wave-packet widths.

The production of indistinguishable partners is challenging, and their generation by independent sources has only recently been achieved in optics (*8*). In one-dimensional quantum conductors, a continuous stream of indistinguishable electrons can be produced by applying a dc voltage bias to two different electronic reservoirs. Because of fermionic statistics, each source fills the electronic states up to the chemical potential $-eV$, and identical electron beams are generated. With the use of such sources, the π exchange phase of indistinguishable fermions has been measured in the above-described collider geometry (*9*) and in a two-particle interferometer based on a Mach-Zehnder geometry (*10*, *11*). However, as these sources generate a continuous beam of electrons, they do not reach the single-particle resolution of their optical analog, and two-particle interference cannot be interpreted as resulting from the overlap between two single-particle wave packets. The manipulation of single-particle states thus requires replacement of dc emitters by triggered ac emitters that generate a single-electron wave packet at a well-defined time.

When dealing with electrons, one can benefit from the charge quantization of a small quantum dot enforced both by Coulomb interaction and fermionic statistics to trigger the emission of particles one by one (*12*–*16*). Moreover, the edge channels of the quantum Hall effect provide an ideal test bench to implement optic-like experiments with electron beams in condensed matter, as electron propagation is ballistic, one-dimensional, and chiral. We will consider here a mesoscopic capacitor (*12*), which comprises a small quantum dot capacitively coupled to a metallic top gate and tunnel coupled to a single edge channel by a quantum point contact of variable transmission D. By applying a square-wave periodic radiofrequency excitation on the top gate, whose

[1]Laboratoire Pierre Aigrain, Ecole Normale Supérieure, CNRS (UMR8551), Université Pierre et Marie Curie, Université Paris Diderot, 24 rue Lhomond, 75231 Paris Cedex 05, France. [2]Université de Lyon, Fédération de Physique André Marie Ampère, CNRS–Laboratoire de Physique de l'Ecole Normale Supérieure de Lyon 46 Allée d'Italie, 69364 Lyon Cedex 07, France. [3]CNRS–Laboratoire de Photonique et de Nanostructures Route de Nozay, 91460 Marcoussis, France.

*To whom correspondence should be addressed. E-mail: feve@lpa.ens.fr